Advanced Energy Conversion Materials
http://ojs.wiserpub.com/index.php/AECM/

UNIVERSAL WISER PUBLISHER

Research Article

Single-Step Green Synthesis of Iron Nanoparticles in the Aqueous Phase for Catalytic Application in Degradation of Malachite Green

Ajay Rathore, Vijay Devra*

Department of Chemistry, Janki Devi Bajaj Government Girls College, Kota, Rajasthan, 324001, India
E-mail: V_devra1@rediffmail.com

Received: 25 September 2021; **Revised:** 29 October 2021; **Accepted:** 02 November 2021

Abstract: The goal of the research was to devise a simple and environment-friendly approach to synthesize iron nanoparticles (FeNPs) and evaluate the catalytic activity of biosynthesized FeNPs for the degradation of the cationic dye Malachite Green (MG) in the presence of Peroxomonosulphate (PMS). Different instrumental approaches were used to characterize green produced FeNPs, and the results show that the NPs are spherical and 48 nm in size. Increasing the concentrations of nanoparticles (0.5×10^{-8} – 2.0×10^{-8} mol/dm^3), Peroxomonosulphate (1.0×10^{-4} – 5.0×10^{-4} mol/dm^3), dye (1.0×10^{-5} – 5.0×10^{-5} mol/dm^3), pH (5), and high temperature (25-35 °C) enhanced the degradation kinetics of MG. Pseudo-first-order kinetics were used to describe the degradation of MG in the FeNPs/PMS system, and activation parameters were derived. The maximum MG degrading efficiency for the FeNPs/PMS system was 88% in 60 minutes under optimum reaction conditions. The structure of intermediates formed by MG degradation by FeNPs/PMS was determined using UV-vis spectrum analysis. The application of synthesized FeNPs to improve Peroxomonosulphate oxidation potential for MG degradation is a unique, efficient, promising, and eco-friendly technology because it does not require any expensive reagents.

***Keywords*:** green synthesis, iron nanoparticles, Peroxomonosulphate, catalysis, Malachite Green

1. Introduction

FeNPs have recently attracted a lot of attention because of their versatile properties, such as high catalytic activities and higher intrinsic reactivity of their surface sites, which have applications in a variety of fields, including the food industry [1], medical science [2], biosensing [3], catalysis [4], magnetic field-assisted separations [5], and analyses [6]. Shape and size of nanoparticles are important properties in their fabrication, processing, and applications due to their large surface area, electron transport, and electrical conductivity that lead to their high catalytic reactivity [7-8].

For the production of iron-based nanoparticles and the modification of their surface properties, many chemical and physical approaches have been established [9]. In physical and chemical procedures, toxic chemicals are used as reducing agents, organic solvents, or non-biodegradable stabilizing agents, making them potentially harmful to the environment and biological systems. The use of microorganisms and plant extracts in the biosynthesis of FeNPs has been suggested as a viable environmentally benign alternative to chemical and physical approaches [10]. Plant extracts commonly contain flavonoids, proteins, terpenoids, polyphenols, and other biomolecules that act as metal ion reducers

DOI: https://doi.org/10.37256/aecm.3120221174

and capping agents to reduce NP aggregation, consequently improving biological potential. The concentration of reactants, time, temperature, and pH are parameters that can be modified during the synthesis to obtain nanoparticles with different properties and applications [11]. Many recent studies have effectively demonstrated the production of FeNPs utilizing natural resources such as *Chlorophytum comosum* leaf extracts [12], *Plantago major* [13], *Mangifera indica*, *Murraya Koenigii*, *Azadirachta indica,* and *Magnolia champaca* [14], *Eucalyptus tereticornis, Melaleuca nesophila,* and *Rosmarinus officinal* [15]. Eucalyptus leaves were utilized to fabricate distinctive green iron polyphenol complex nanoparticles [16]. FeNPs are amorphous materials with a ferric ion situated in nanoparticles chelated by plant polyphenols, according to an X-ray Absorption Spectroscopy (XAS) analysis. Here we choose the plant extract approach for FeNPs production because of its unique properties and multifunctional applications.

Dyes are a particular subject of concern among organic pollutants, due to their complex structure and persistence. They are difficult to decompose using conventional treatment procedures. Adsorption and flocculation, which are common dye effluent treatment techniques, are inefficient because they produce solid residue, which causes other environmental issues and needs further treatment [17-19]. Transition metal-related oxidative methods have demonstrated increased removal efficiency for the degradation of carcinogenic pollutants into lower molecular weight and reduced toxicity [20-21]. The results of NPs-treated textile wastewater revealed that some major compounds were greatly diminished, bio-transformed, or completely degraded [22-23]. The most effective chemical oxidation approach is an advanced oxidation technology, which is already gaining significant application in the water treatment process [24]. Activated persulfate oxidation, one of the AOPs, has recently received a lot of attention because of the comparatively long lifetime of the sulfate radicals (SO_4^{2-}, E_0 = 2.5 – 3.1 V) and the moderate reaction conditions [25]. Heat [26], ultrasound [27], and transition metal [28]-generated sulfate radicals are extremely powerful oxidizing species, as indicated by the fact that sulfate-containing compounds are the most effective oxidants. The catalytic activity and oxidation state of transition metals influence the formation of reactive species such as sulfate radicals. A sulfate radical-based mechanism was suggested when manganese, cobalt, copper, nickel, and silver transition metals were used [29-34], and the same was suggested as one of the most efficient pathways when iron transition metal was used [35].

We developed an effective, eco-friendly, and convenient green technique for the synthesis of FeNPs from their salt using leaf extract from the Indian medical plant Azadirachta indica (A. Indica), popularly known as neem, which belongs to the Meliaceae family. Synthesized FeNPs were used to degradation an MG dye solution to test their catalytic activity. The synthesis and applicability of the *A. Indica* synthesized FeNPs was used as a catalyst in nitro-phenol reduction [15]. According to our best knowledge from A. Indica synthesized FeNPs has not yet been explored in the degradation of MG. In the dye industry, MG is classified as a triarylmethane dye and is used to color silk, paper, and leather. When MG is released into receiving streams, it has adverse effects on aquatic life, including the liver, gills, kidney, intestine, and pituitary gonadotrophic cells [36]. As a result, the removal of colored synthetic organic dyestuff from waste effluents is essential for the environment. The primary goals of this study are as follows: i) To synthesis stable FeNPs using a simple green approach; the low cost of this technology will be appealing for combating waterborne disease and public health. ii) Studied the effect of different experimental conditions on the morphology of nanoparticles. iii) Evaluate the effect of reactant concentrations, pH, temperature, and other conditions on MG degradation. iv) Propose MG degradation pathway in the FeNPs/PMS system.

2. Material and method

2.1 *Chemical and materials*

MG (Sigma-Aldrich), Peroxomonosulphate ($2KHSO_5KHSO_4K_2SO_4$ 95%) (Sigma-Aldrich), silver nitrate ($AgNO_3$) (E. Merck), and other reagents such as H_2SO_4, NaOH, Na_2SO_4 were of analytical grade. In Kota, Rajasthan, India, the *A. Indica (neem)* plant was chosen. The plant leaves extract was prepared by boiling 10 g of leaves in 100 ml of water for 20 minutes at 80 °C. The extract was then vacuum-filtered and stored at 4 °C for subsequent testing.

2.2 *Instrumentation*

For measurements and characterizations, Scanning Electron Microscopy (SEM, Nova Nano FE-SEM 450 (FEI), US) and transmission electron microscopy (TEM, Tecnai G2 20 (FEI) S-Twin, US) at 200 kV were used to analyze

morphological characteristics. Dispersed NPs were centrifuged and ultra-sonicated for 40 minutes, following which 30 L aliquots were taken and placed on the stub for SEM study, and the ultra-sonicated dispersed suspension was mounted on a standard carbon-coated Cu grid and dried under an IR lamp for TEM investigation. The functional groups on the surface of FeNPs were investigated using the Fourier-transform infrared spectroscopy (FTIR), ALPHA-T Bruker, Germany. A 1% (w/w) sample was mixed with 100 mg of KBr powder and pressed into a sheer slice for FTIR measurement. For each measurement, an average of 32 scans with a resolution of 4 cm^{-1} was recorded. Analyses using a Peltier accessory (temperature-controlled) attached to a spectrophotometer (3000 + LAB INDIA) with a resolution of 1 nm were used to confirm completion of bio-reduction of the $FeCl_3$ solution and conduct a degradation study.

2.3 *Iron nanoparticle synthesis*

For the synthesis process, an aqueous solution of 1.0×10^{-3} mol/dm^3 $FeCl_3$ was prepared, heated at 60 °C in an oil bath with magnetic stirring, and dropwise 15% leaf extracts were added in a round bottom flask. The reaction solution color steadily changed from light yellowish to brownish-black within 60 minutes, confirming the bio-reduction of Fe^{+3} ions into FeNPs. The resultant dispersion was centrifuged for 15 minutes, and the supernatant was stored at 4 °C. Different spectrophotometric techniques were used to confirm the formation of FeNPs. The influence of various precursor salt ($FeCl_3$) concentrations and leaf extract percentages in the synthesis process was also examined.

2.4 *Kinetic measurements*

The desired concentration of MG prepared in aqueous solution and requisite quantity of MG, FeNPs with other reactants placed in Erlenmeyer flask at 30 °C. A known volume of PMS aqueous solution was used to initiate the reaction. The kinetics were monitored using the absorbance of MG measured spectrophotometrically at max 618 nm at a regular time interval. It was noticed that as time passes, the absorbance of the dye solution decreases, indicating that the dye is degrading. At 618 nm, Beer's law was seen over a concentration range of (1×10^{-5} to 1×10^{-4} mol/dm^3), and the MG molar absorptivity index was calculated to be 2730 ± 50 mol^{-1} dm^3 cm^{-1} [37]. The relationship between Log(C/C0) and time was found to be linear, confirming pseudo-first-order kinetics. The progress of the reaction measures at least 80% of the reaction.

3. Results and discussion

3.1 *Metal nanoparticle characterization results*

UV-Visible absorbance spectroscopy has proven to be a very helpful tool for analyzing metal nanoparticles. Because nanoparticles have a high surface area to volume ratio, the surface plasmon resonance frequency is particularly sensitive to the shape and size of nanoparticles. The UV-Visible spectra of samples were recorded at different time intervals for color change during the synthesis of FeNPs as presented in Figure1 (inset). Previous research has also observed similar color variations [38]. A dark brown color appeared after 60 minutes together with a high SPR peak having maximum absorption at 258 nm which proves the formation of FeNPs (Figure 1) [39]. It is also evident that the small increase in absorbance turns light brown color to dark brown, which indicates the formation of a nanocluster of zero-valent FeNPs. The optical band gap was determined by the UV-visible spectrum of nanoparticle suspensions applied Tauc expression 4.81 ev. The Tauc expression for direct transition is given by $\alpha h\upsilon = B\,(h\upsilon - E_g)^m$ where α is absorption coefficient, B is constant having different values for different transitions, E_g is the band gap energy, $h\upsilon$ is the energy of a photon and m is an exponent depending upon the electronic transition. For this study, the linear portion of the plot between $(\alpha h\upsilon)^2$ versus $h\upsilon$ taking n = 2 (for allowed direct transition band gap) where n = 1/m, was extrapolated to obtain the optical band gap [20]. The band gap energies partially depend on the crystallinity of the sample, as the band energies of the crystallized samples are compared with crystallized bulk materials. The band gap energies are higher than the corresponding bulk materials. The findings can also be affected by synthesis procedure, nature of reactants, and reaction conditions [40]. SEM and TEM analysis confirmed the morphology of synthesized FeNPs as shown in Figures 2(a) and 2(b). SEM images confirm the nanoparticles are grown with well-defined morphology and almost in a spherical shape [41]. FeNPs are well isolated from one another in the TEM micrograph, indicating effective capping by water-

soluble biomolecules present in the A. Indica leaves extract with spherical and size of 48 nm. Biomolecules are known to bind to the surface of FeNPs, considerably increasing their surface charge and improving their stability by preventing aggregation [42].

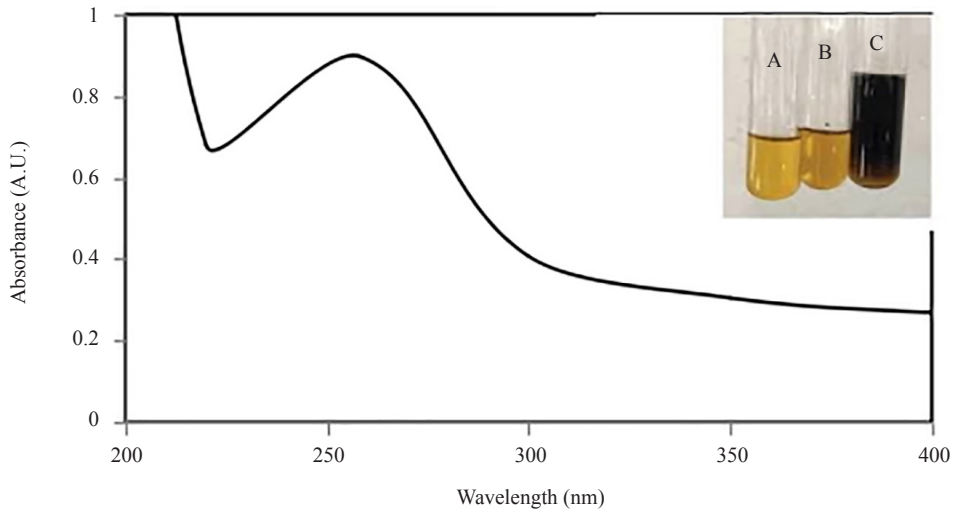

Figure 1. The color change of the dispersion photographs and the UV-Visible absorption spectra of FeNPs

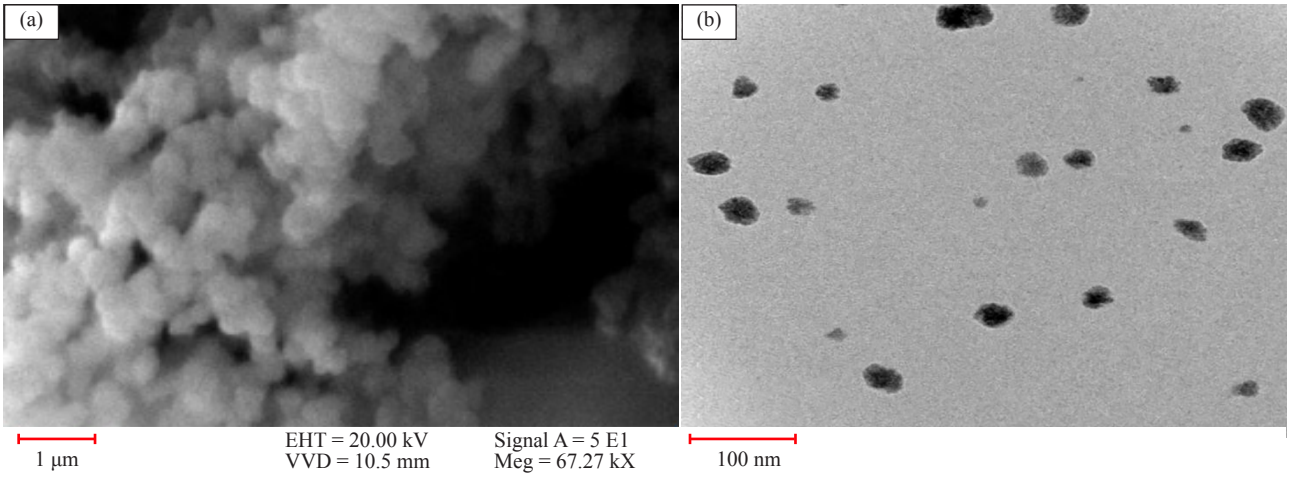

Figure 2. SEM [a], TEM [b] images of synthesized FeNPs at optimum reaction condition ($FeCl_3$ = 1.0 × 10^{-3} mol/dm^3, leaf Extract = 15%, pH = 6.0 and Temp = 60 °C)

3.1.1 *Effect of leaf extract's percentage*

UV-visible absorbance spectroscopy was used to investigate the effect of different leaf extract percentages in the synthesis process. With a higher percentage of leaf extract, the absorption peak becomes broader. A weak absorption peak at wavelength 258 nm was seen at a low percentage of leaf extract (5%), which could be due to insufficient ferrous ion reduction. As the quantity of leaf extract increases up to 15%, the intensity of the absorption peak increases [43]. A plot of the reaction conversion rate versus different percentages of leaf broth confirmed this effect (Figure 3). The results revealed that the reaction conversion rate increases with the leaf extract percentage up to 15%, beyond which there is no obvious growth trend, indicating colloidal FeNPs agglomeration at higher leaf extract percentages. A secondary

reduction process happens on the surface of the performed nucleus due to the unusually large number of biomolecules present, causing the particle size to increase [34]. In a conclusion, the ideal leaf extract percentage for the generation of FeNPs is 15%.

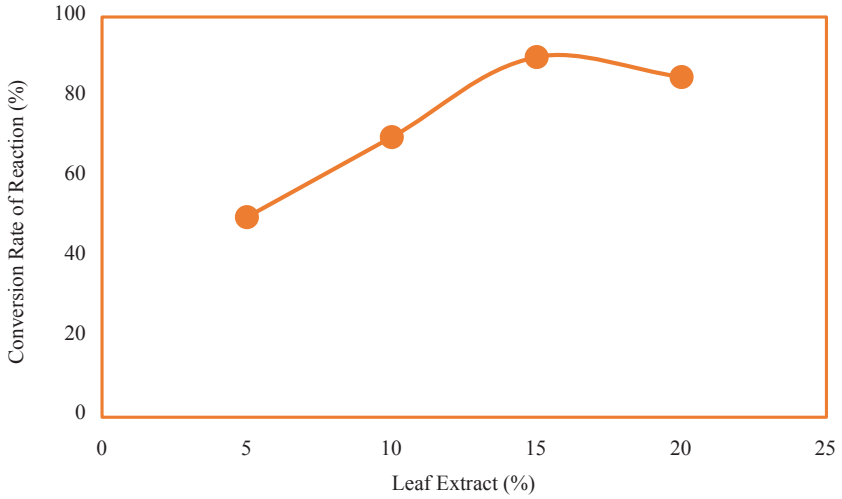

Figure 3. Effect of different percentages of leaf extract on the conversion rate of reaction at constant [$FeCl_3$] = 1.0 × 10^{-3} mol/dm^3, pH = 6.0, and Temperature = 60 °C

3.1.2 *Effect of precursor salt concentration*

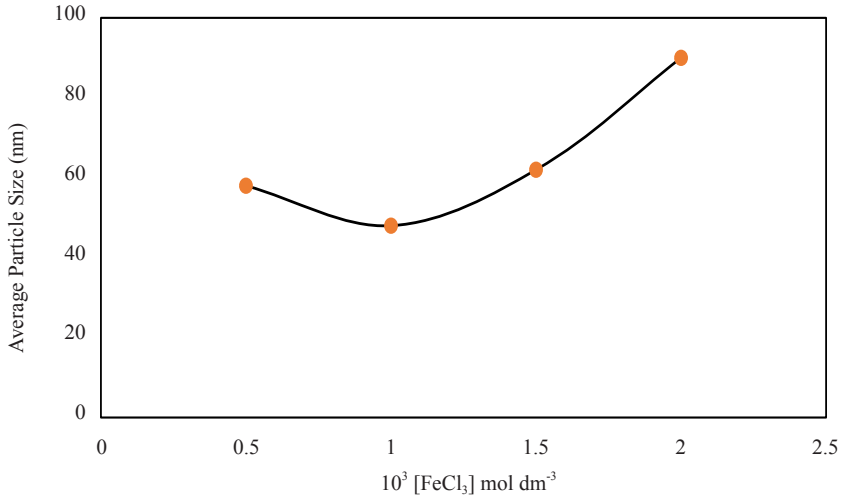

Figure 4. Effect of different concentrations of iron salt (0.5 × 10^{-3} mol/dm^3 to 2.0 × 10^{-3} mol/dm^3) on average particle size of FeNPs at leaf extract = 15%, pH = 6.0 and Temperature = 60 °C

The influence of iron chloride concentrations between 0.5 × 10^{-3} mol/dm^3 to 2.0 × 10^{-3} mol/dm^3 on the formation of FeNPs was investigated in this work. The size of green produced FeNPs is greatly dependent on the precursor salt concentration. It was confirmed that when the concentration of $FeCl_3$ was increased from 0.5 × 10^{-3} mol/dm^3 to 1.0 × 10^{-3} mol/dm^3, the particle size of NPs decreased. The particle size grew, as the salt concentration was increased (Figure 4). The number of iron nuclei grows as the concentration of precursor salt increases, while the particle size decreases.

However, at high reactant concentrations, an excess number of nuclei is formed, resulting in the increase of nuclei aggregation and particle size. Similarly, Huang et al. observed aggregation of nanoparticles in the reduction of ferrous ions using green tea extract [44]. Therefore, the optimum concentration of precursor salt is 1.0×10^{-3} mol/dm^3 for the synthesis of FeNPs.

3.1.3 *Stability of FeNPs*

The stability of nanoparticles dispersion is a key factor in their application including the extremely sensitive to oxygen and colloidal agglomeration [45]. A. Indica leaves extract was used as a reducing as well as capping agent without any other special capping agents in this work to avoid contamination of other organic compounds. The dispersion of FeNPs stabilized by aqueous leaves extract was centrifuged for 15 minutes. The supernatant obtained by centrifugation was stored at 4 °C, and no precipitation or sedimentation was seen even after one month, indicating long-term stability of the Fe colloids as prepared. It indicates the biomolecules included in the leaves extract of A. Indica, such as flavonoids, terpenoids, and polyphenols, stabilized FeNPs. The possible equation for the synthesis of FeNPs are

$$Fe^{+2} + \text{A. Indica leaf extract} \xrightarrow[60\ ^\circ C]{\text{Stirring}} [\text{Fe/A. Indica leaf extract}]^{+2} \quad (1)$$

$$[\text{Fe/A. Indica leaf extract}]^{+2} \xrightarrow[60\ ^\circ C]{\text{Stirring for 60 min}} [\text{Fe/A. Indica leaf extract}] \quad (2)$$

The leaf extract combines with Fe^{+2} to generate the $[Fe/A.\ Indica\ leaf\ extract]^{+2}$ complex when A. Indica leaf broth is added to ferric chloride solution (Equation 1). After that, this complex reacts with a functional group of biomolecules present in A. Indica leaf extract to produce [Fe/A. Indica leaf extract] (Equation 2). The synthesized nanoparticles capped by biomolecules of leaves extract are also confirmed by FTIR results (Figure 5). The O-H and C = C stretching vibrations are responsible for the absorption bands detected at 3393 cm^{-1} and 1627 cm^{-1}, respectively. C-O-C and absorption peaks are related to the band that emerges at 1076 cm^{-1} [15]. The germinal methyl groups are generally allocated to a band at 1384 cm^{-1}. According to the findings, through the interaction with electron or carbonyl groups, flavonoids could be adsorbed on the surfaces of metal nanoparticles. The synthesis of bio-capped FeNPs could be attributed to the presence of reducing sugar in the leaf extract.

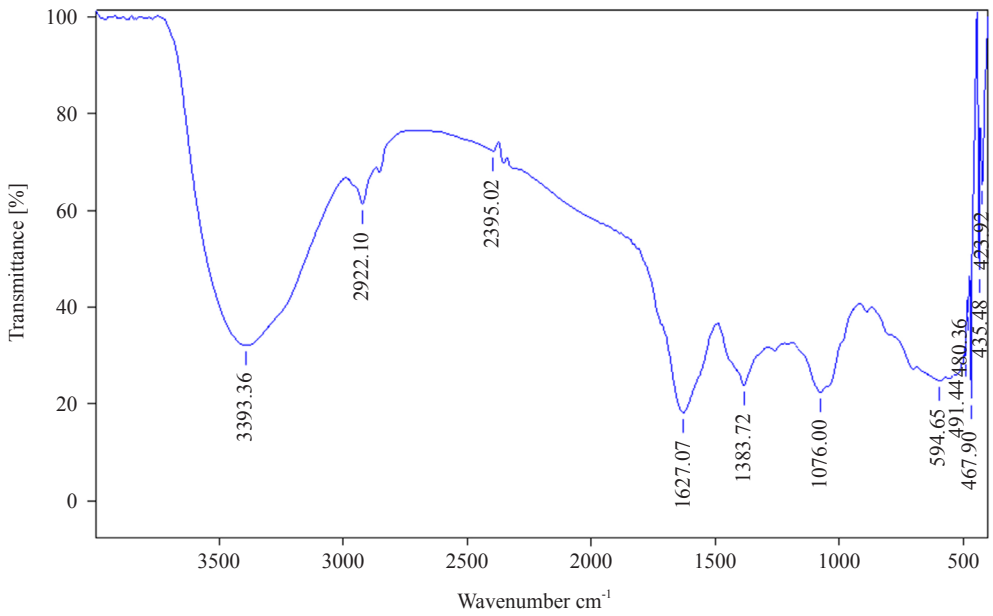

Figure 5. FT-IR Spectra of green synthesized FeNPs

3.2 *Effect of experimental conditions on the degradation process*

3.2.1 *UV-visible spectra of intermediates and degradation pathway*

The capability of the green-produced FeNPs to catalyze MG was exceptional. The chemical features and structural changes of MG degradation reaction within 60 minutes were illustrated by the UV-visible absorption spectrum (Figure 7). The absorbance spectrum of MG has three distinct peaks, the greatest of which is at 618 nm. During the degradation process, this peak undergoes a blue shift, which has been linked to the nonselective attack of reactive oxygen species on C-N bonds [46]. The lowering of the peaks at 312 and 425 nm indicates the complete degradation of the conjugated chromophore structure dye molecule [47]. The production of 4-(dimethylamino) benzophenone is indicated by a small increase in absorbance between 340-360 nm [46-47]. The identification of a degradation route that culminates in monosubstituted aromatic rings and end products is also noteworthy. The following path is proposed based on observed results obtained from spectrum changes during MG degradation (Figure 6).

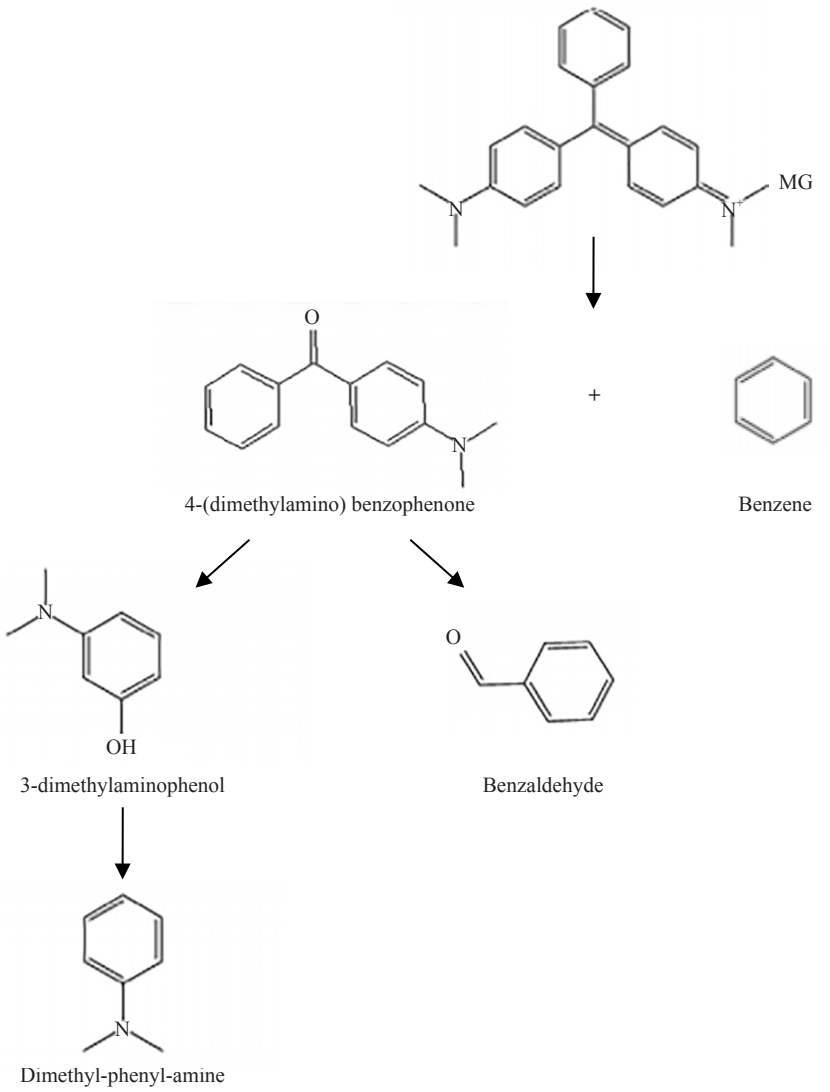

Figure 6. Proposed oxidative degradation route of MG in FeNPs/PMS system

Yong et al. reported that MG degradation might be initiated by two mechanisms: 1) hydroxyl radical attack on

the central carbon of MG, or 2) N-demethylation or deamination of MG [47]. MG reacted with the produced hydroxyl radicals in this FeNPs/PMS study, generating 4-(dimethylamino) benzophenone and 3-dimethylaminophenol by combining PMS and FeNPs through the first pathway. In the photocatalytic degradation of MG dye, a benzophenone has also been found as a degradation product [48]. The current investigation finds none of the chemicals linked to the second mechanism suggested by Yong et al. [47].

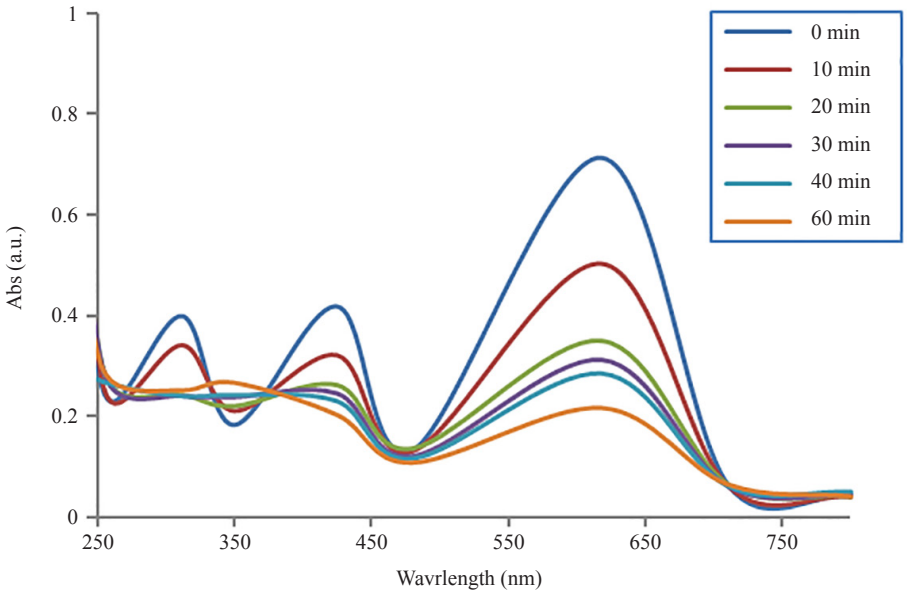

Figure 7. In the FeNPs/PMS system, the UV-vis spectrum shifts with reaction time ([PMS] = 5×10^{-4} mol/dm^3, [MG] = 5×10^{-5} mol/dm^3, [FeNPs] = 1×10^{-8} mol/dm^3, pH = 3.0 and Temperature 30 °C).

3.2.2 *Dye dependence*

At 30 °C, the initial concentration of MG varied from 1.0×10^{-5} to 1.0×10^{-4} mol/dm^3, whereas the concentrations of the other reactants and reaction conditions remain constant. The rate of degradation was shown to increase when the concentration of MG in the FeNPs/PMS system increased. This could be attributed to an increase in dye concentration, which enhanced the reaction rate because there were more dye molecules available to degrade. The degradation rate was reduced after a particular concentration of dye (5×10^{-5} mol/dm^3) was reached (Table 1). This can be explained by the fact that the availability of $SO_4^{\bullet}$ radicals is reduced at constant oxidant concentrations, resulting in the greatly decreased MG decomposition [49].

3.2.3 *Peroxomonosulphate (PMS) dependence*

The degradation experiment was carried out with FeNPs at various concentrations of PMS (1.0×10^{-4} to 1.0×10^{-3} mol/dm^3) and constant concentrations of other reactants and conditions. The oxidant Peroxomonosulphate is usually applied in advanced oxidation processes based on sulfate radicals and has a standard redox potential of E° = 1.82 V. The $SO^{4\bullet}$ radicals (SRs) based mechanism dominates PMS, and radicals are generated by catalytic activation of PMS (Equation 3).

$$2HSO_5^- + Fe° \rightarrow Fe\ (II) + 2SO_4^{\bullet -} + 2OH^- \quad (3)$$

Sulfate radicals (SRs) are generated and degrade MG molecules quickly, converting them to products. When the concentration of PMS rises, the rate of degradation rises as well. The findings imply that as oxidant concentrations rise, the number of SRs rises, increasing the rate of oxidation Fe° to Fe^{2+} ion, therefore, improving MG oxidative degradation.

The degradation rate increases until the PMS concentration reaches 5.0×10^{-4} mol/dm^3, after which it remains constant at higher PMS concentrations, showing that the active sites of fixed catalyst concentration gradually become the limiting factor (Table 1) [50].

3.2.4 *Effect of initial pH*

The initial pH of the solution is significant in dye degradation because pH changes the surface charge properties of the catalyst. MG degradation was studied at several initial pH solution values ranging from 3 to 9, which were adjusted with either 0.1 mol/dm^3 HCl or 0.1 mol/dm^3 NaOH. The findings show that at acidic pH, the rate of degradation is faster (Table 1). In a previous study employing nano valent iron to degrade azo dyes, a similar pattern was observed [51]. At lower pH which has more H+ ions, FeNPs can donate electrons to more ions, converting them to atoms. These atoms then attack the dye molecule, which eventually degrades.

Table 1. Effect of variation of [PMS] [MG] and pH an oxidative degradation of MG at 30 °C

S.No.	10^4[PMS] mol/dm^3	10^5[MG] mol/dm^3	10^8[FeNPs] mol/dm^3	pH	10^4K_{obs} (sec^{-1})
1	1.0	5.0	1.0	3.0	0.50
2	2.5	5.0	1.0	3.0	1.25
3	5.0	5.0	1.0	3.0	2.15
4	7.5	5.0	1.0	3.0	2.20
5	10.0	5.0	1.0	3.0	2.21
6	5.0	1.0	1.0	3.0	1.15
7	5.0	2.5	1.0	3.0	1.80
8	5.0	5.0	1.0	3.0	2.15
9	5.0	7.5	1.0	3.0	2.00
10	5.0	10.0	1.0	3.0	1.60
11	5.0	5.0	1.0	3.0	2.15
12	5.0	5.0	1.0	5.0	2.0
13	5.0	5.0	1.0	7.0	1.6
14	5.0	5.0	1.0	9.0	1.0

3.2.5 *FeNPs and temperature dependence*

FeNPs catalytic activity was evaluated in a PMS system with MG at concentrations ranging from 0.5×10^{-8} to 2.0×10^{-8} mol/dm^3 at three different temperatures: 25, 30, and 35 °C. To demonstrate the catalytic activity, a graph is shown between the concentration of FeNPs and the rate constant obtained at three different temperatures. The graph shows that as the concentration of FeNPs increased, more active sites on the surface of Fe^o were available for PMS to occupy, allowing for the generation of more reactive species (Figure 8) [28]. As a result, the rate of MG degradation was enhanced as the temperature increased. The value of the energy of activation (20.41 kJ/mol^1) was calculated from the plot of log (k_{obs}) versus 1/T.

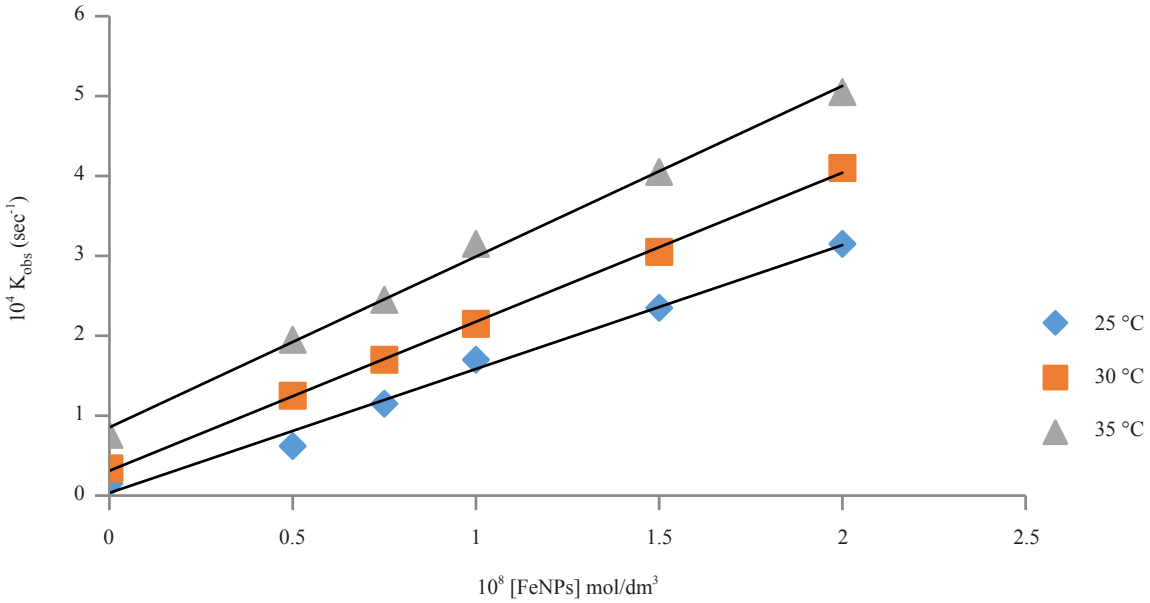

Figure 8. Effect of [FeNPs] on degradation rate of MG at three Temperature and Fixed [PMS] = 5×10^{-4} mol/dm^3 [MG] = 5×10^{-5} mol/dm^3 and pH = 3.0

3.2.6 *Effect of ionic strength*

The zeta potential of colloidal particles in water is affected by ionic strength. The outer sphere interaction between particles and solute can be affected as ionic strength increases. Covalent and ionic bonding, on the other hand, are well defined, and inner-sphere complexation is rarely affected [52]. At a constant concentration of reactants, the ionic strength was varied by varying concentrations of sodium sulfate (0.3 – 3.0) × 10^{-4} mol/dm^3 at 30 °C. The results show that in the Fe/PMS system, ionic strength did not affect MG degradation. As a result, the inner sphere interaction between HSO_5^- and the active site on the Fe^o Surface was confirmed to be the catalytic reaction route.

3.2.7 *Mechanism*

Sulfate ions have longer life due to their reaction occurring via the electron transfer process [53]. The high reactivity of the sulfate anion can be contributed to its redox partner bisulfate/sulfate ions ability as a leaving group separation and purification technology. Therefore, this property of sulfate radicals may be useful to the degradation of dyeing wastewater. Based on the findings of the kinetic degradation investigation, it can be concluded that the oxidative degradation of MG dye in the presence of FeNPs by PMS is a radical-based mechanism, with sulfate radical ions ($SO_4^{\bullet -}$) being formed during catalytic activation of HSO_5^- (PMS). The catalyst's role as a mediator for electron transfer to PMS has also been documented [28]. The plausible mechanism in support of the observed kinetics is as below.

$$2HSO_5^- + Fe^\circ \rightarrow Fe(II) + 2SO_4^{\bullet -} + 2OH^-$$

$$2SO_4^{\bullet -} + Fe(II) + MG \rightarrow Products + Fe^\circ$$

$$2HSO_5^- + MG \xrightarrow{Fe^\circ} Products + 2OH^-$$

4. Conclusion

The current study shows that *A. Indica* leaf extract can produce extremely stable FeNPs that can be used as a reducing and capping agent. Therefore, synthesized FeNPs have stability for one month at 4 ^{o}C temperature without any protecting gas. The above experimental results reveal that the synthesis of FeNPs by bio-reduction of iron salt was highly dependent on process factors such as leaf extract concentration and iron salt concentration. The characterization results suggest that synthesized FeNPs were nano-sized and in a spherical shape. FT-IR spectroscopy was used to investigate the reduction and stabilization processes induced by the functional groups of *A. Indica* extract. The optimal conditions for the synthesis of FeNPs are 1.0×10^{-3} mol/dm^3 iron salt concentration and 15% leaf extract at 60 °C temperature. The FeNPs were effective for activating PMS and producing sulfate radicals, which were applied to degrade the MG dye. The rate of MG degradation increases as the catalyst, PMS concentration, and temperature are increased. According to the findings, FeNPs have a lot of potential for dye degradation technologies.

Acknowledgments

The Department of Science and Technology of India funded our institution's FIST Laboratory for experimental study, as well as MNIT Jaipur for SEM and TEM analysis of FeNPs synthesis.

Conflict of interest statement

The authors declare no competing financial interest.

References

[1] Bentahir Y, Elmarhoum S, Salghi R, Algarra M, Ríos A, Zougagh M. Dispersed synthesis of uniform Fe_3O_4 magnetic nanoparticles via in situ decomposition of iron precursor along cotton fibre for Sudan dyes analysis in food samples. *Food Additives & Contaminants: Part A*. 2017; 34(11): 1853-1862. Available from: https://doi.org/10.1080/19440049.2017.1357840.

[2] Silva AKA, Espinosa A, Kolosnjaj-Tabi J, Wilhelm C, Gazeau F. Medical applications of iron oxide nanoparticles. *Iron Oxides: From Nature to Applications*. 2016; 12: 425-472. Available from: https://doi.org/10.1002/9783527691395.ch18.

[3] Hasanzadeh M, Shadjou N, de la Guardia M. Iron and iron-oxide magnetic nanoparticles as signal-amplification elements in electrochemical biosensing. *TrAC Trends in Analytical Chemistry*. 2015; 72: 1-9. Available from: https://doi.org/10.1016/j.trac.2015.03.016.

[4] Beheshtkhoo N, Kouhbanani MAJ, Savardashtaki A, Amani AM, Taghizadeh S. Green synthesis of iron oxide nanoparticles by aqueous leaf extract of Daphne mezereum as a novel dye removing material. *Applied Physics A*. 2018; 124(5): 1-7. Available from: https://doi.org/10.1007/s00339-018-1782-3.

[5] Massoud A, Mahmoud H. Evaluation of hybrid polymeric resin containing nanoparticles of iron oxide for selective separation of In (III) from Ga (III). *Journal of Inorganic and Organometallic Polymers and Materials*. 2017; 27(6): 1806-1815. Available from: https://doi.org/10.1007/s10904-017-0645-2.

[6] Cao M, Li Z, Wang J, Ge W, Yue T, Li R, et al. Food related applications of magnetic iron oxide nanoparticles: enzyme immobilization, protein purification, and food analysis. *Trends in Food Science & Technology*. 2012; 27(1): 47-56. Available from: https://doi.org/10.1016/j.tifs.2012.04.003.

[7] Ikram M, Hussain I, Hassan J, Haider A, Imran M, Aqeel M, et al. Evaluation of antibacterial and catalytic potential of copper-doped chemically exfoliated boron nitride nanosheets. *Ceramics International*. 2020; 46(13): 21073-21083. Available from: https://doi.org/10.1016/j.ceramint.2020.05.180.

[8] Ikram M, Tabassum R, Qumar U, Ali S, Ul-Hamid A, Haider A, et al. Promising performance of chemically exfoliated Zr-doped MoS_2 nanosheets for catalytic and antibacterial applications. *RSC Advances*. 2020; 10(35): 20559-20571. Available from: https://doi.org/10.1039/D0RA02458A.

[9] Zhang WX. Nanoscale iron particles for environmental remediation: an overview. *Journal of nanoparticle*

Research. 2003; 5(3): 323-332. Available from: https://doi.org/10.1023/A:1025520116015.
[10] Sadhasivam S, Vinayagam V, Balasubramaniyan M. Recent advancement in biogenic synthesis of iron nanoparticles. *Journal of Molecular Structure*. 2020; 1217: 128372. Available from: https://www.sciencedirect.com/science/article/abs/pii/S0022286020306979.
[11] Yew YP, Shameli K, Miyake M, Khairudin NBB, Mohamad SEB, Naiki T, et al. Green biosynthesis of superparamagnetic magnetite Fe_3O_4 nanoparticles and biomedical applications in targeted anticancer drug delivery system: A review. *Arabian Journal of Chemistry*. 2020; 13(1): 2287-2308. Available from: https://doi.org/10.1016/j.arabjc.2018.04.013.
[12] Ardakani LS, Alimardani V, Tamaddon AM, Amani AM, Taghizadeh S. Green synthesis of iron-based nanoparticles using Chlorophytum comosum leaf extract: methyl orange dye degradation and antimicrobial properties. *Heliyon*. 2021; 7(2): e06159. Available from: https://doi.org/10.1016/j.heliyon.2021.e06159.
[13] Lohrasbi S, Kouhbanani MA, Beheshtkhoo N, Ghasemi Y, Amani AM, Taghizadeh S. Green synthesis of iron nanoparticles using plantago major leaf extract and their application as a catalyst for the decolorization of azo dye. *BioNanoScience*. 2019; 9(2): 317-322. Available from: https://doi.org/10.1007/s12668-019-0596-x.
[14] Karthikeyan C, Ranjani M, Kim AR, Yoo DJ. Synthesis of iron nanoparticles using Azadirachta indica extract and its catalytic activity toward nitrophenol reduction. *Journal of Nanoscience and Nanotechnology*. 2016; 16(3): 2527-2533. Available from: https://doi.org/10.1166/jnn.2016.10793.
[15] Wang Z, Fang C, Megharaj M. Characterization of iron-polyphenol nanoparticles synthesized by three plant extracts and their fenton oxidation of azo dye. *ACS Sustainable Chemistry & Engineering*. 2014; 2(4): 1022-1025. Available from: https://doi.org/10.1021/sc500021n.
[16] Wang Z. Iron complex nanoparticles synthesized by eucalyptus leaves. *ACS Sustainable Chemistry & Engineering*. 2013; 1(12): 1551-1554. Available from: https://doi.org/10.1021/sc400174a.
[17] Bashir MS, Jiang X, Kong XZ. Porous polyurea microspheres with Pd immobilized on surface and their catalytic activity in 4-nitrophenol reduction and organic dyes degradation. *European Polymer Journal*. 2020; 129: 109652. Available from: https://doi.org/10.1016/j.eurpolymj.2020.109652.
[18] Bashir MS, Jiang X, Yang X, Kong XZ. Porous polyurea supported Pd catalyst: Easy preparation, full characterization, and high activity and reusability in reduction of hexavalent chromium in aqueous system. *Industrial & Engineering Chemistry Research*. 2021; 60(22): 8108-9119. Available from: https://doi.org/10.1021/acs.iecr.1c01376.
[19] Rout DR, Jena HM. Removal of malachite green dye from aqueous solution using reduced graphene oxide as an adsorbent. *Materials Today: Proceedings*. 2021; 47: 1173-1182. Available from: https://doi.org/10.1016/j.matpr.2021.03.406.
[20] Zhao Z, Liu J, Tai C, Zhou Q, Hu J, Jiang G. Rapid decolorization of water soluble azo-dyes by nanosized zero-valent iron immobilized on the exchange resin. *Science in China Series B: Chemistry*. 2008; 51(2): 186-192. Available from: https://doi.org/10.1007/s11426-007-0121-x.
[21] Ikram M, Raza A, Imran M, Ul-Hamid A, Shahbaz A, Ali S. Hydrothermal synthesis of silver decorated reduced graphene oxide (rGO) nanoflakes with effective photocatalytic activity for wastewater treatment. *Nanoscale Research Letters*. 2020; 15(1): 1-11. Available from: https://doi.org/10.1186/s11671-020-03323-y.
[22] Rout DR, Jena HM. Synthesis of novel reduced graphene oxide decorated β-cyclodextrin epichlorohydrin composite and its application for Cr(VI) removal: Batch and fixed-bed studies. *Separation and Purification Technology*. 2021; 278: 119630. Available from: https://doi.org/10.1016/j.seppur.2021.119630.
[23] Devi KN, Devi SA, Singh WJ, Singh KJ. Nickel doped zinc oxide with improved photocatalytic activity for malachite green dye degradation and parameters affecting the degradation. *Journal of Materials Science: Materials in Electronics*. 2021; 32(7): 8733-8745. Available from: https://doi.org/10.1007/s10854-021-05545-x.
[24] Xia X, Zhu F, Li J, Yang H, Wei L, Li Q, et al. A review study on sulfate-radical-based advanced oxidation processes for domestic/industrial wastewater treatment: degradation, efficiency, and mechanism. *Frontiers in Chemistry*. 2020; 8: 592056. Available from: https://doi.org/10.3389/fchem.2020.592056.
[25] Ren W, Zhou Z, Zhu Y, Jiang L, Wei H, Niu T, et al. Effect of sulfate radical oxidation on disintegration of waste activated sludge. *International Biodeterioration & Biodegradation*. 2015; 104: 384-390. Available from: https://doi.org/10.1016/j.ibiod.2015.07.008.
[26] Yanga S, Wang P, Yang X, Shan L, Zhang W, Shao X, et al. Degradation efficiencies of azo dye Acid Orange 7 by the interaction of heat, UV and anions with common oxidants: persulfate, peroxymonosulfate and hydrogen peroxide. *Journal of Hazardous Materials*. 2010; 179(1-3): 552-558. Available from: https://doi.org/10.1016/j.jhazmat.2010.03.039.
[27] Su S, Guo W, Yi C, Leng Y, Ma Z. Degradation of amoxicillin in aqueous solution using sulphate radicals under

ultrasound irradiation. *Ultrasonics sonochemistry*. 2012; 19(3): 469-474. Available from: https://doi.org/10.1016/j.ultsonch.2011.10.005.
[28] Nagar N, Devra V. Activation of peroxodisulfate and peroxomonosulfate by green synthesized copper nanoparticles for methyl orange degradation: A kinetic study. *Journal of Environmental Chemical Engineering*. 2017; 5(6): 5793-5800. Available from: https://doi.org/10.1016/j.jece.2017.11.014.
[29] Xiong X, Sun B, Zhang J, Gao N, Shen J, Li J, et al. Activating persulfate by Fe^0 coupling with weak magnetic field: performance and mechanism. *Water Research*. 2014; 62: 53-62. Available from: https://doi.org/10.1016/j.watres.2014.05.042.
[30] Huang J, Zhang H. Mn-based catalysts for sulfate radical-based advanced oxidation processes: A review. *Environment International*. 2019; 133: 105141. Available from: https://doi.org/10.1016/j.envint.2019.105141.
[31] Ji Y, Kong D, Lu J, Jin H, Kang F, Yin X, et al. Cobalt catalyzed peroxymonosulfate oxidation of tetrabromobisphenol A: kinetics, reaction pathways, and formation of btgydtcvuyinhiurominated by-products. *Journal of Hazardous Materials*. 2016; 313: 229-237. Available from: https://doi.org/10.1016/j.jhazmat.2016.04.033.
[32] Nagar N, Devra V. Green synthesis and characterization of copper nanoparticles using Azadirachta indica leaves. *Materials Chemistry and Physics*. 2018; 213: 44-51. Available from: https://doi.org/10.1016/j.matchemphys.2018.04.007.
[33] Murugavelu M, Andal P, Shailaja S, Ramachandran MS. Kinetic studies on the reaction between nickel(II) lactate and peroxomonosulphate ion-The effect of formaldehyde. *Journal of Molecular Catalysis A: Chemical*. 2009; 306(1-2): 1-5. Available from: https://doi.org/10.1016/j.molcata.2009.02.012.
[34] Nagar N, Jain S, Kachhawah P, Devra V. Synthesis and characterization of silver nanoparticles via green route. *Korean Journal of Chemical Engineering*. 2016; 33(10): 2990-2997. Available from: https://doi.org/10.1007/s11814-016-0156-9.
[35] Xia X, Zhu F, Li J, Yang H, Wei L, Li Q, et al. A review study on sulfate-radical-based advanced oxidation processes for domestic/industrial wastewater treatment: degradation, efficiency, and mechanism. *Frontiers in Chemistry*. 2020; 8. Available from: https://doi.org/10.3389/fchem.2020.592056.
[36] Srivastava S, Sinha R. Roy D. Toxicological effects of malachite green. *Aquatic Toxicology*. 2004; 66(3): 319-329. Available from: https://doi.org/10.1016/j.aquatox.2003.09.008.
[37] Mirila D, Pirvan M, Platon N, Georgescu A, Zichil V, Nistor I. Activated adsorption on clay of micropollutants from paper printing industry. Scientific Study & Research. *Chemistry & Chemical Engineering, Biotechnology, Food Industry*. 2018; 19(1): 63-72. Available from: https://www.proquest.com/openview/7a1be1e17fc11653f430827f0a58138b/1?pq-origsite=gscholar&cbl=716381.
[38] Nath D, Manhar AK, Gupta K, Saikia D, Das SK, Mandal M. Phytosynthesized iron nanoparticles: effects on fermentative hydrogen production by Enterobacter cloacae DH-89. *Bulletin of Materials Science*. 2015; 38(6): 1533-1538. Available from: https://doi.org/10.1007/s12034-015-0974-0.
[39] Ebrahiminezhad A, Taghizadeh S, Ghasemi Y, Berenjian A. Green synthesized nanoclusters of ultra-small zero valent iron nanoparticles as a novel dye removing material. *Science of the Total Environment*. 2018; 621: 1527-1532. Available from: https://doi.org/10.1016/j.scitotenv.2017.10.076.
[40] Momeni MM, Ghayeb YJ. Synthesis and characterization of iron-doped titania nanohoneycomb and nanoporous semiconductors by electrochemical anodizing method as good visible light active photocatalysts. *Journal of Materials Science: Materials in Electronics*. 2015; 26(7): 5509-5517. Available from: https://doi.org/10.1007/s10854-015-3108-y.
[41] Xiao C, Li H, Zhao Y, Zhang X, Wang X. Green synthesis of iron nanoparticle by tea extract (polyphenols) and its selective removal of cationic dyes. *Journal of Environmental Management*. 2020; 275: 111262. Available from: https://doi.org/10.1016/j.jenvman.2020.111262.
[42] Veeramanikandan V, Madhu GC, Pavithra V, Jaianand K, Balaji P. Green synthesis, characterization of iron oxide nanoparticles using Leucas aspera leaf extract and evaluation of antibacterial and antioxidant studies. *International Journal of Agriculture Innovations and Research*. 2017; 6(2): 242-250.
[43] Hernandez-Hernandez AA, Aguirre-Alvarez G, Carino-Cortes R, Mendoza-Huizar LH, Jimenez-Alvarado R. Iron oxide nanoparticles: synthesis, functionalization, and applications in diagnosis and treatment of cancer. *Chemical Papers*. 2020; 74: 3809-3824. Available from: https://doi.org/10.1007/s11696-020-01229-8.
[44] Huang L, Luo F, Chen Z, Megharaj M, Naidu R. Green synthesized conditions impacting on the reactivity of Fe NPs for the degradation of malachite green. *Spectrochimica Acta Part A: Molecular and Biomolecular Spectroscopy*. 2015; 137: 154-159. Available from: https://doi.org/10.1016/j.saa.2014.08.116.
[45] Jain S, Jain A, Kachhawah P, Devra V. Synthesis and size control of copper nanoparticles and their catalytic application. *Transactions of Nonferrous Metals Society of China*. 2015; 25(12): 3995-4000. Available from: https://

doi.org/10.1016/S1003-6326(15)64048-1.
[46] Ju Y, Qiao J, Peng X, Xu Z, Fang J, Yang S, et al. Photodegradation of malachite green using UV-vis light from two microwave-powered electrodeless discharge lamps (MPEDL-2): further investigation on products, dominant routes and mechanism. *Chemical Engineering Journal*. 2013; 221: 353-362. Available from: https://doi.org/10.1016/j.cej.2012.06.055.
[47] Yong L, Zhang G, Yuefei J, Xiaobin H, Cheng S, Shaogui Y, et al. Photodegradation of malachite green under simulated and natural irradiation: kinetics, products, and pathways. *Journal of Hazardous Materials*. 2015; 285: 127-136. Available from: https://doi.org/10.1016/j.jhazmat.2014.11.041.
[48] Navarro P, Zapata JP, Gotor G, Gonzalez-Olmos R, Gomez-Lopez VM. Degradation of malachite green by a pulsed light/H2O2 process. *Water Science and Technology*. 2019; 79(2): 260-269. Available from: https://doi.org/10.2166/wst.2019.041.
[49] Wu J, Zhang H, Qiu J. Degradation of Acid Orange 7 in aqueous solution by a novel electro/Fe^{2+}/peroxydisulfate process. *Journal of Hazardous Materials*. 2012; 215: 138-145. Available from: https://doi.org/10.1016/j.jhazmat.2012.02.047.
[50] Huang YH, Huang YF, Huang CI, Chen CY. Efficient decolorization of azo dye Reactive Black B involving aromatic fragment degradation in buffered Co^{2+}/PMS oxidative processes with a ppb level dosage of Co^{2+}-catalyst. *Journal of Hazardous Materials*. 2009; 170(2-3): 1110-1118. Available from: https://doi.org/10.1016/j.jhazmat.2009.05.091.
[51] Rahman N, Abedin Z, Hossain MA. Rapid degradation of azo dyes using nano-scale zero valent iron. *American Journal of Environmental Sciences*. 2014; 10(2): 157. Available from: https://doi.org/10.3844/ajessp.2014.157.163.
[52] Stumm W. *Chemistry of the solid-water interface: processes at the mineral-water and particle-water interface in natural systems*. John Wiley & Son Inc.; 1992.
[53] Lu J, Zhou Y, Lei J, Ao Z, Zhou Y. Fe_3O_4/graphene aerogels: A stable and efficient persulfate activator for the rapid degradation of malachite green. *Chemosphere*. 2020; 251: 126402. Available from: https://doi.org/10.1016/j.chemosphere.2020.126402.